

1  
2  
3  
4 **Mechanical and electrical properties of low SWNT content 3YTZP**  
5 **composites**  
6

7 R. Poyato<sup>1,\*</sup>, J. Macías-Delgado<sup>1,2</sup>, A. García-Valenzuela<sup>1,2</sup>, Á. Gallardo-López<sup>1,2</sup>,  
8 A. Morales-Rodríguez<sup>1,2</sup>, A. Muñoz<sup>2</sup>, A. Domínguez-Rodríguez<sup>2</sup>.  
9

10  
11  
12 <sup>1</sup> *Inst. Ciencia de Materiales de Sevilla (CSIC-Univ. Sevilla), Avda. Américo Vespucio*  
13 *49, 41092 Sevilla (Spain).*  
14

15 <sup>2</sup> *Dep. Física de la Materia Condensada, Univ. de Sevilla, apdo. 1065, 41080 Sevilla*  
16 *(Spain).*  
17  
18

19  
20 **Abstract**  
21

22  
23 Fully dense 3 mol% Y<sub>2</sub>O<sub>3</sub>-ZrO<sub>2</sub> (3YTZP) composites with low single wall carbon  
24 nanotube content (0.5, 1 and 1.5 vol% SWNT) were prepared by colloidal processing  
25 and Spark Plasma Sintering. SWNT were distributed at ceramic grain boundaries and  
26 also into agglomerates. Characterization of SWNT agglomerates indicated that increase  
27 in SWNT vol% does not imply an increase in agglomeration. SWNT agglomerate  
28 density was related to the evolution of hardness and fracture toughness with SWNT  
29 vol%. Electrical properties of the composites were characterized in a wide temperature  
30 range, and percolation threshold was estimated. A model allowing separation of the  
31 individual SWNT bundles contribution to resistance from the resistance due to junctions  
32 between bundles was proposed for composites with a percolating SWNT network.  
33  
34  
35  
36  
37  
38  
39  
40  
41  
42  
43  
44  
45  
46  
47

48 **Keywords:** composites; carbon nanotubes; processing; mechanical properties; electrical  
49 properties  
50  
51

52  
53  
54  
55 

---

\* Corresponding author.

56 E-mail address: rosalia.poyato@icmse.csic.es

57 Phone number: +34 954 48 95 34

58 FAX number: +34 954 46 06 65  
59  
60  
61  
62  
63  
64  
65

## Introduction

Within the past 20 years, the scientific and engineering communities have paid great attention to carbon nanotubes (CNTs) due to their attractive properties. CNTs can show a Young's modulus up to 1.2 TPa, a tensile strength around a hundred times higher than steel and an elevated resilience. They also possess tunable surface properties, well-defined hollow interiors, and can be either metallic or semiconducting depending on diameter and chirality.<sup>1,2</sup> Based on these fascinating properties, many potential applications such as scanning probe tips, drug delivery systems, electronic devices, sensors and actuators, high-strength composites, catalyst support, field emission displays, transparent conducting films, and so on were proposed.<sup>3,4</sup> In these years, both the research articles and patents on this area increased rapidly. Recently, Zhang *et al.*<sup>5</sup> analyzed the publications topic tendency from 2001 to 2011, showing the study of composites with CNTs to be one of the emerging areas, with an increase from 13 to 27% of the total publications. Interest in these composites is based on the possibility of transferring some of the attractive properties of CNTs to the resulting composites<sup>6</sup>.

Among advanced ceramics, yttria-doped zirconia is considered a technologically interesting material due to its superior mechanical properties and good ionic conductivity.<sup>7,8</sup> In recent years, several works were devoted to the study of zirconia/CNTs composites, pursuing an enhancement of the mechanical properties. However, up to date, this enhancement has not been clearly demonstrated. A decrease of Vickers hardness when increasing CNT content was reported by different authors,<sup>9-13</sup> even for composites with low CNT vol%.<sup>14-16</sup> Although some authors related this effect to the observed decrease in composite density when increasing CNT content,<sup>9,11</sup> it has been also reported for fully densified composites with SWNT contents up to 10 vol%.<sup>13</sup>

1  
2  
3  
4 The decreasing trend was also linked to higher presence of agglomerated CNTs<sup>17</sup> in  
5  
6 composites with high amount of nanotubes, since it is assumed that agglomeration  
7  
8 becomes more relevant due to dispersion difficulties during processing.<sup>18</sup> However,  
9  
10 recent investigations on Al<sub>2</sub>O<sub>3</sub>/SWNT composites have pointed out that the presence of  
11  
12 agglomerates does not play a fundamental role on the decrease in hardness.<sup>19</sup> On the  
13  
14 contrary, it was rather explained by the presence of higher SWNT quantities at the grain  
15  
16 boundaries. The detachment between SWNTs within thick bundles has been pointed out  
17  
18 as the origin of the lower fracture toughness obtained for high SWNT content  
19  
20 3YTZP/SWNT composites when compared to monolithic ceramic.<sup>13</sup> In this context, the  
21  
22 study of low SWNT vol% composites, in order to assess whether a lower SWNT content  
23  
24 at the grain boundaries results in an enhancement of the mechanical properties, appears  
25  
26 as a challenge.  
27  
28  
29  
30

31 The study of the electrical properties of ceramic/CNT composites has recently  
32  
33 also come into focus, as adding CNTs to a ceramic matrix also modify the electrical  
34  
35 conductivity of the resulting composite. Most of the studies have focused on the  
36  
37 analysis of the electrical percolative behaviour,<sup>11,16,20-26</sup> since a step raise in electrical  
38  
39 conductivity is the common trend observed in composites once percolation of the CNT  
40  
41 network is achieved. Percolation thresholds from 0.64 to 5.5 vol% have been published  
42  
43 for composites with alumina or zirconia matrix.<sup>11,16,21-25</sup> This wide range of reported  
44  
45 values can be related to the different processing techniques used to prepare the  
46  
47 materials. Shin and Liang<sup>22,23</sup> and Fonseca *et al.*<sup>24</sup> reported percolation thresholds of 5.5  
48  
49 and 3 vol% CNTs for 3 mol% Y<sub>2</sub>O<sub>3</sub>-ZrO<sub>2</sub>/MWNT and 8 mol% Y<sub>2</sub>O<sub>3</sub>-ZrO<sub>2</sub>/SWNT  
50  
51 composites, respectively. In these studies, composite powders were processed by ball  
52  
53 milling the mixture of CNTs and ceramic powder. Recently, composites obtained from  
54  
55 powders prepared in a similar way have been shown to present a high amount of CNT  
56  
57  
58  
59  
60  
61  
62  
63  
64  
65

1  
2  
3  
4 agglomerates,<sup>27</sup> which would result in a lower CNT content at the ceramic grain  
5  
6 boundaries than the nominal one. Thus, a higher amount of CNT would be required in  
7  
8 order to achieve a percolating network, resulting in an overestimated percolation  
9  
10 threshold. These results highlight the need to correlate the CNT agglomerate density  
11  
12 and the percolation threshold in ceramic/CNT composites.  
13  
14

15         Regarding the ac conductivity on ceramic/CNT composites, the published  
16  
17 studies are scarce.<sup>24-26</sup> Only Fonseca *et al.*<sup>24</sup> and González-Julián *et al.*<sup>26</sup> reported  
18  
19 electrical properties in ac conditions in a wide temperature range. A mixed ionic-  
20  
21 electronic conductivity was described for 8 mol% Y<sub>2</sub>O<sub>3</sub>-ZrO<sub>2</sub>/SWNT composites.<sup>24</sup>  
22  
23 Charge transport along the nanotube shells and hopping conduction across nanotube-  
24  
25 nanotube junctions were suggested as the two contributions to electrical conductivity in  
26  
27 Si<sub>3</sub>N<sub>4</sub>/MWNT composites.<sup>26</sup> To the best of our knowledge, studies on ac conductivity  
28  
29 and charge transport contributions in 3YTZP/SWNT composites have not been  
30  
31 published up to date.  
32  
33  
34

35         In this paper, 3 mol% yttria doped zirconia composites containing low SWNT  
36  
37 content (0.5, 1 and 1.5 vol%) were prepared by a combination of aqueous colloidal  
38  
39 processing and Spark Plasma Sintering, with the aim of obtaining a homogeneous  
40  
41 SWNT distribution throughout the ceramic matrix and minimizing the presence of  
42  
43 agglomerates. The SWNT agglomerate density was characterized and related to the  
44  
45 evolution of hardness and fracture toughness with SWNT vol%. Electrical properties of  
46  
47 the composites were characterized in a wide temperature range. Conductivity  
48  
49 measurements at room temperature allowed determination of the percolation threshold.  
50  
51 Modelling of the impedance properties of the composite with a percolating SWNT  
52  
53 network was carried out, and an equivalent circuit which separates the individual  
54  
55  
56  
57  
58  
59  
60  
61  
62  
63  
64  
65

1  
2  
3  
4 SWNT bundles resistance contribution from the resistance due to junctions between  
5  
6 bundles was proposed.  
7  
8  
9

## 10 **2. Experimental procedure**

### 11 **Raw materials and processing**

12  
13  
14  
15 Monolithic polycrystalline 3YTZP and SWNT/3YTZP composites with different  
16  
17 carbon nanotube content (0.5, 1 and 1.5 vol%) were prepared from 3 mol% yttria  
18  
19 stabilized tetragonal zirconia powder (3YTZP, 40 nm particle size and 99% purity)  
20  
21 supplied by Nanostructured and Amorphous Materials Inc. (Houston, TX) and HIP-co  
22  
23 purified SWNTs provided by Carbon Solutions Inc. (Riverside, CA). Acid treatment of  
24  
25 the SWNTs was carried out using a mixture of concentrated sulfuric acid (98%) and  
26  
27 nitric acid (70%) in the ratio 3:1, with the aim of disentangle and cut the raw SWNTs  
28  
29 ropes.<sup>28</sup> This treatment also introduces carboxyl groups on the walls and ends of  
30  
31 SWNTs enabling their dispersion in basic medium. SWNTs were suspended in the acid  
32  
33 mixture for 24 h at room temperature and the suspension was sonicated for 8 h. SWNTs  
34  
35 were collected on ~20 nm pore alumina filter membranes, washed in high purity ethanol  
36  
37 for several times and freeze-dried in order to avoid possible re-agglomeration.  
38  
39  
40  
41  
42

43 Colloidal processing of composite powders with the different SWNT contents  
44  
45 was carried out using ammonia solution as a basic medium.<sup>28</sup> Ceramic powder and acid-  
46  
47 treated SWNT suspensions were subjected to ultrasonic agitation using a sonication  
48  
49 bath before and after mixing. Composite powder blends were dried on a hot plate  
50  
51 assisted by stirring, and pH and homogeneity were controlled during the process.  
52  
53 Finally, composite powders were homogenized in an agate mortar.  
54  
55  
56  
57  
58

### 59 **Ceramic sintering**

1  
2  
3  
4 SPS (Model 515S, SPS Dr Sinter Inc., Kanagawa, Japan) was used to sinter the  
5  
6 materials in a 15-mm diameter cylindrical graphite die/punch setup in vacuum  
7  
8 atmosphere. The sintering processes were carried out at 1250 °C with a hold time at  
9  
10 peak temperature of 5 min, under uniaxial pressure of 75 MPa. Heating and cooling  
11  
12 rates were 300 and 50 °C/min, respectively. Bulk densities were measured using  
13  
14 Archimedes' method, with distilled water as immersion medium. Theoretical density  
15  
16 values for composites were calculated by the rule of mixtures assuming density values  
17  
18 of 6.10 g·cm<sup>-3</sup> for 3YTZP and 1.80 g·cm<sup>-3</sup> for SWNTs.  
19  
20  
21  
22  
23

#### 24 **Microstructural, mechanical and electrical characterization**

25  
26 Structural integrity of SWNTs in the composites after SPS sintering was  
27  
28 assessed by Raman spectroscopy on fracture surfaces using a dispersive microscope  
29  
30 (Horiba Jobin Yvon LabRam HR800, Kyoto, Japan) equipped with a 20 mW He-Ne  
31  
32 green laser (532.14 nm). The microscope used a 100x objective and a confocal pinhole  
33  
34 of 100 μm. The Raman spectrometer was calibrated using a silicon wafer.  
35  
36  
37

38  
39 Microstructural studies of composites fracture and polished surfaces were  
40  
41 performed by high-resolution scanning electron microscopy (HR-SEM), using a Hitachi  
42  
43 S5200 microscope (Hitachi High-Technologies America Inc., USA), to analyze the  
44  
45 distribution of SWNTs in the 3YTZP matrix, and to characterize the ceramic grains  
46  
47 morphology. Distribution and morphology of SWNT agglomerates were characterized  
48  
49 by low magnification conventional SEM (Model JEOL 6460LV, JEOL USA Inc., MA,  
50  
51 USA). Cross section slices, i.e. surfaces parallel to the SPS pressing direction were  
52  
53 polished with diamond paste up to 1 μm for morphological studies. Additionally,  
54  
55 polished surfaces devoted to characterize the 3YTZP grains were thermally etched at  
56  
57 1200 °C for 20 min in air to reveal grain boundaries. The morphology characterization  
58  
59  
60  
61  
62  
63  
64  
65

1  
2  
3  
4 was made measuring 200 grains or agglomerates, respectively, to obtain the equivalent  
5  
6 planar diameter as size parameter,  $d$  (or  $D$ )= $2(\text{area}/\pi)^{1/2}$ , and the shape factor,  $f$  (or  
7  
8  $F$ )= $(4\pi \cdot \text{area})/(\text{perimeter})^2$ . Standard deviation of distributions was also evaluated.  
9  
10 Hereafter, lowercase letters will refer to 3YTZP grains parameters and uppercase letters  
11  
12 to agglomerates ones. Agglomerate surface density was evaluated from the area fraction  
13  
14 covered by them in low magnification SEM micrographs. *ImageJ* software was used for  
15  
16 morphological analysis.  
17  
18

19  
20 Vickers indentation tests were carried out to evaluate the hardness and fracture  
21  
22 toughness of sintered 3YTZP and composites at room temperature. Tests were  
23  
24 performed on sample surfaces polished to 1  $\mu\text{m}$  diamond paste using a Vickers indenter  
25  
26 with a range of loads up to 2 kgf (Duramin Struers, Germany). Twelve indents were  
27  
28 made on each sample avoiding boundary effects (i.e. keeping the appropriate distance  
29  
30 from sample edges and between indentations marks) and were analyzed using a  
31  
32 confocal microscope LEICA DCM 3D. Vickers hardness,  $H_v$ , was calculated from the  
33  
34 indentation load,  $P$ , and the diagonal of Vickers imprints,  $a$ :  $H_v=1.854(P/a^2)$ .  
35  
36  
37

38 Fracture toughness,  $K_{IC}$ , was calculated by using the equation given by Anstis *et*  
39  
40 *al.*<sup>29</sup> where  $c$  is the crack length measured from the centre of the imprint and  $E$  the  
41  
42 elastic modulus. **The crack length was measured 24 h after the indentation, once the**  
43  
44 **cracks were fully developed.**  
45  
46

$$47 \quad K_{IC} = 0.016 \left( \frac{E}{H_v} \right)^{1/2} \left( \frac{P}{c^{3/2}} \right) \quad (1)$$

48  
49  
50  
51

52 Electrical characterization was carried out by Impedance Spectroscopy using an  
53  
54 Agilent 4294A analyzer in the frequency range from 100 to  $2 \times 10^6$  Hz, at temperatures  
55  
56 from 25 to 450 °C. Measurements were carried out in argon atmosphere to avoid  
57  
58 oxidation of the samples and subsequent degradation of the SWNTs during the process.  
59  
60  
61  
62  
63  
64  
65

1  
2  
3  
4 Colloidal silver paste was applied on both sides of the samples and electrodes were fired  
5  
6 at 600 °C for 30 min under argon flow. Equivalent circuit approach was adopted for the  
7  
8 data analysis with fitted curve using Z-view software and equivalent circuit model.  
9

### 10 11 12 13 **3. Results and discussion**

#### 14 15 *3.1 Microstructural characterization*

16  
17 Table 1 displays the density values together with the global results of  
18  
19 morphological parameters of as-sintered samples. A full densification was obtained in  
20  
21 all the sintered materials. Similar mean grain size (~230 nm) and shape factor (~0.75)  
22  
23 were measured in the different composites and no significant differences were observed  
24  
25 compared to monolithic zirconia grains, except for slightly narrower size distributions  
26  
27 (smaller  $\sigma_{<d>}$ ).  
28  
29

30  
31 Fig. 1 shows the Raman spectra measured in the composites, monolithic 3YTZP  
32  
33 ceramic and as-received SWNTs. The composites spectra show SWNT characteristic  
34  
35 radial breathing mode (RBM) band near 150–200  $\text{cm}^{-1}$  and G-band near 1500–1600  
36  
37  $\text{cm}^{-1}$ . **In the G-band it can be observed the lower-frequency broad shoulder**  
38  
39 **centred around 1570  $\text{cm}^{-1}$  (Breit-Wigner-Fano or BWF lineshape), which is**  
40  
41 **characteristic of metallic SWNT<sup>28</sup>.** The composites spectra are very similar to the  
42  
43 SWNT spectrum before processing of the composites, clearly confirming the absence of  
44  
45 significant damage to SWNTs during powder processing and sintering. **A G-band shift**  
46  
47 **towards higher frequencies, by  $\sim 20 \text{ cm}^{-1}$ , is observed in the three composites,**  
48  
49 **which can be attributed to residual stresses in the SWNTs imposed by the**  
50  
51 **constraining ceramic matrix<sup>28</sup>.** D-band (centred on 1350  $\text{cm}^{-1}$ ), associated to  
52  
53 disordered graphite and crystalline defects, is also observed.  $I_D/I_G$  ratio calculations give  
54  
55 similar values for the three composites (6.6, 6.5 and 7.2% for 0.5, 1 and 1.5 vol%  
56  
57  
58  
59  
60  
61  
62  
63  
64  
65



1  
2  
3  
4 SWNT, respectively) pointing to a similar amount of crystalline defects in the  
5  
6 nanotubes. On the other hand, peaks at 165, 260, 320, 465, 610, and 643  $\text{cm}^{-1}$  are  
7  
8 observed in the spectra acquired in the composites, corresponding to the six Raman  
9  
10 bands theoretically predicted for tetragonal zirconia.<sup>30</sup>  
11

12  
13 HR-SEM micrographs of characteristic fracture surfaces of the composites are  
14  
15 presented in Fig. 2. SWNT bundles are located at the ceramic grain boundaries and  
16  
17 debonded CNTs from the matrix can also be observed. Whereas the 3YTZP grains  
18  
19 surrounded by SWNT bundles are scarce in the composite with 0.5 vol% SWNT (fig  
20  
21 2(a)), the amount of SWNT bundles at the grain boundaries increases in the composites  
22  
23 with higher SWNT vol% (figures 2(b) and 2(c)). CNTs are mainly well distributed on  
24  
25 the 3YTZP matrix; however, some agglomerates are also found in these high-resolution  
26  
27 observations. The presence of these agglomerates or clusters has been previously  
28  
29 reported in CNT/ceramic matrix composites.<sup>13,19,27,31,32</sup>  
30  
31  
32

33  
34 Low-magnification SEM micrographs (Fig. 3) illustrate the arrangement and  
35  
36 morphology of SWNT agglomerates in the studied composites. The maximum  
37  
38 agglomerate size ranges from 30 to 60  $\mu\text{m}$  (Table 2), which is similar to previously  
39  
40 published values for  $\text{Al}_2\text{O}_3/\text{MWNT}$  composites also prepared by colloidal processing<sup>32</sup>.  
41  
42 Although it is assumed that the tendency of forming agglomerates is due to Van der  
43  
44 Waals interactions between nanotubes, they are not expected to lead to such important  
45  
46 agglomerate sizes in composites with a rather low SWNT content<sup>32</sup> as in this study.  
47  
48 Other forces that might play a key role in the behaviour of the 3YTZP/SWNT powder  
49  
50 mixtures have been suggested, and it was shown from thermodynamic considerations  
51  
52 that long, thin rods mixed with spheres can induce phase separation and demixion<sup>32</sup>.  
53  
54  
55

56  
57 Similar mean agglomerate size, about 7–9  $\mu\text{m}$ , and a marked elongation ( $F \sim$   
58  
59 0.45) are found for the three composites. These morphological characteristics are similar  
60  
61  
62  
63  
64  
65

1  
2  
3  
4 to those reported by Morales-Rodríguez *et al.*<sup>19</sup> for Al<sub>2</sub>O<sub>3</sub>/SWNT composites prepared  
5  
6 by a similar processing route. These authors showed that SWNT agglomerates are  
7  
8 flattened structures strongly aligned on the direction perpendicular to the SPS  
9  
10 compression axis.

11  
12  
13 An increase in the agglomerate surface density  $\rho_s$  is observed when increasing  
14  
15 SWNT vol% (Table 2). Nevertheless, this fact does not imply an increase of the  
16  
17 percentage of the total SWNT content that is agglomerated, A%. Assuming that the area  
18  
19 fraction covered by agglomerates in SEM micrographs is equal to its volume fraction in  
20  
21 composites ( $\rho_s = \rho_v$ , Delesse's principle of stereology), this percentage can be estimated  
22  
23 as:  
24  
25

$$26 \quad A\% = 100 \rho_v / \text{SWNT vol\%} \quad (2)$$

27  
28  
29 Despite the increase in agglomerate volume fraction for higher SWNT vol%,  
30  
31 similar percentages of agglomerated SWNTs (~ 30%) from the total SWNT content  
32  
33 have been found in the three composites. So an increase in SWNT content does not  
34  
35 imply an increase in agglomeration.  
36  
37

38  
39 The SWNT vol% contained in the agglomerates (A-SWNT) and distributed at  
40  
41 the grain boundaries (GB-SWNT) can be directly inferred from agglomerate volume  
42  
43 density as:  
44

$$45 \quad A\text{-SWNT} = \rho_v \quad (3)$$

$$46 \quad GB\text{-SWNT} = \text{SWNT vol\%} - A\text{-SWNT} \quad (4)$$

47  
48  
49 As it is shown in Table 2, after colloidal processing and sintering, the real  
50  
51 content of nanotubes at the grain boundaries are estimated to be 0.32, 0.74 and 1.1  
52  
53 SWNT vol% for composites with 0.5, 1, and 1.5 nominal SWNT vol%, respectively.  
54  
55

56  
57 It is interesting to note that lower A-SWNT vol% has been achieved in these  
58  
59 materials in comparison with Al<sub>2</sub>O<sub>3</sub>/SWNT composites with similar SWNT content.<sup>19</sup>  
60  
61  
62  
63  
64  
65

1  
2  
3  
4 Whereas 60% of the SWNT are contained in agglomerates in Al<sub>2</sub>O<sub>3</sub>/1 vol% SWNT  
5  
6 composites,<sup>19</sup> only 26% of SWNT are agglomerated in our 3YTZP composites with the  
7  
8 same SWNT content. Although similar processing routines were used in both studies,  
9  
10 SWNT freeze-drying after acid-treatment was introduced in the present work with the  
11  
12 aim of obtaining a more homogeneous SWNT distribution.<sup>16,33</sup> It is clear that, although  
13  
14 it is not possible to reduce the maximum or the mean agglomerate size by freeze-drying  
15  
16 the nanotubes instead of drying on a hot plate, a decrease of the percentage of the CNT  
17  
18 content that are agglomerated is achieved.  
19  
20  
21  
22  
23

### 24 *3.2 Mechanical properties*

25  
26 Similar Vickers hardness,  $H_v$ , values within the experimental error are obtained  
27  
28 for the three composites and the monolithic 3YTZP ceramic (Table 3). To the best of  
29  
30 our knowledge, absence of decrease or increase of hardness with increasing CNT  
31  
32 content in ceramic matrix composites has only been reported for Al<sub>2</sub>O<sub>3</sub> with 1 vol%  
33  
34 SWNT composites,<sup>34</sup> since most of the authors report a decrease of hardness, even for  
35  
36 composites with low CNT content.<sup>11,14-16</sup> The decreasing trend reported by previous  
37  
38 authors for 3YTZP/CNT composites is shown in Figure 4(a). This tendency is usually  
39  
40 linked to a decrease in the composite density,<sup>11</sup> an increase in nanotube agglomeration<sup>17</sup>  
41  
42 or a weakening of interfacial bonding when the grains are wrapped by CNT and,  
43  
44 therefore, the direct contact area and bonding force among grains decrease with  
45  
46 increasing CNT content.<sup>12,13</sup> In this study, fully densified composites have been  
47  
48 obtained, and the increase in the surface density of agglomerates (Table 2) does not play  
49  
50 a fundamental role in the evolution of hardness when increasing SWNT content. Thus,  
51  
52 it is clear that the incorporation of low SWNT content in the ceramic matrix minimizes  
53  
54  
55  
56  
57  
58  
59  
60  
61  
62  
63  
64  
65

1  
2  
3  
4 the SWNT weakening effect on interfacial cohesion between ceramic grains observed in  
5  
6 composites with high SWNT content.<sup>13</sup>  
7  
8

9  
10 **Regarding the fracture toughness values, in recent years, there have been**  
11 **different arguments about the validity of the Vickers indentation technique to**  
12 **characterize fracture toughness of CNT-ceramic matrix composites, and it has**  
13 **been suggested that it should be measured by the single-edge notched beam**  
14 **(SENB) method<sup>6,10,35,36</sup>. Some authors have compared the results obtained in**  
15 **ceramic matrix composites using the indentation method with the ones obtained**  
16 **with the SENB test and, although the absolute values of  $K_{IC}$  measured by both**  
17 **tests differ (higher values obtained from indentation measurements), a similar**  
18 **trend was observed when measuring using the two techniques<sup>35,36</sup>. Taking this**  
19 **result into account, and considering also the simplicity of the indentation test and**  
20 **the difficulty of obtaining bars for SEBN test from SPS disks in several studies, it**  
21 **has been proposed that, although the  $K_{IC}$  values obtained from indentation tests**  
22 **are not fully quantitative, they can be used to compare different compositions**  
23 **tested in a same study, or for comparison purpose with previous works.**  
24  
25  
26  
27  
28  
29  
30  
31  
32  
33  
34  
35  
36  
37  
38  
39  
40

41 **Figure 4(b) shows that the obtained  $K_{IC}$  data follow a increasing trend for**  
42 **the composites with increasing SWNT vol.%. These values are similar<sup>11,14,15</sup> to**  
43 **previously published results (also obtained from Vickers indentation tests) for**  
44 **3YTZP composites with low SWNT content.** This slight enhancement is consequence  
45  
46  
47  
48 of toughening mechanisms present in the composites, such as CNT crack bridging and  
49 pull out, and CNT ropes debundling and uncoiling, as described by previous authors.<sup>6</sup>  
50  
51  
52  
53  
54  
55  
56

### 57 *3.3 Electrical properties*

58  
59  
60  
61  
62  
63  
64  
65

1  
2  
3  
4 A room temperature conductivity of  $6 \times 10^{-6} \text{ S} \cdot \text{cm}^{-1}$  was measured on the  
5  
6 composite with 1.5 vol% SWNT (Table 3). On the contrary, monolithic 3YTZP ceramic  
7  
8 and composites with 0.5 and 1 vol% SWNT were found to be electrically isolating with  
9  
10 a very high room temperature resistivity. The percolation threshold of the carbon  
11  
12 nanotubes in the 3YTZP matrix is therefore between 1 and 1.5 vol%. Nevertheless,  
13  
14 considering the agglomerates characterization presented above (Table 2), the real  
15  
16 percolation threshold would be between 0.74 and 1.1 vol% SWNT (real SWNT content  
17  
18 at grain boundaries), values that are comparable to those published in literature for  
19  
20  $\text{Al}_2\text{O}_3/\text{MWNT}$  composites (0.64-1 vol%).<sup>20,21,25,32</sup>  
21  
22  
23

24 The percolation threshold obtained in this study is lower than the published one  
25  
26 by Shin and Liang<sup>22,23</sup> for 3YTZP/MWNT composites (~5.5 vol%). This is probably  
27  
28 consequence of the processing efforts devoted in this study to minimize the presence of  
29  
30 SWNT agglomerates in the composites, which lead to a higher amount of SWNT  
31  
32 distributed in the ceramic grain boundaries.  
33  
34

35 Impedance complex plane plots corresponding to the composite with 1.5 vol%  
36  
37 SWNT from room temperature up to 180 °C, are shown in Fig. 5(a). A single impedance  
38  
39 arc can be observed until 180 °C, when a second arc appears at lower frequency.  
40  
41 According to Garrett *et al.*<sup>37</sup> the impedance properties of a SWNT percolating network  
42  
43 can be modelled with an equivalent circuit consisting of two R-C elements in series. It  
44  
45 has been published that the resistance of the carbon nanotube bundles and the resistance  
46  
47 of the junctions between these bundles are the two major contributions to SWNT  
48  
49 network resistance,<sup>26,38,39</sup> and it is well established that the resistance across junctions is  
50  
51 higher than the resistance through the bundles themselves.<sup>38,39,40</sup> Thus, the lower  
52  
53 resistance element in the equivalent circuit model can be assigned to the CNT bundles  
54  
55 whereas the higher resistance one can be assigned to the junctions.  
56  
57  
58  
59  
60  
61  
62  
63  
64  
65

1  
2  
3  
4 In this context, we have modelled the single impedance arc obtained from room  
5  
6 temperature to 160 °C (arc not shown) using an equivalent circuit model (inset in Fig.  
7  
8 5(a)) similar to the described one by previous authors,<sup>37,41</sup> consisting of a R-C element  
9  
10 connected in series with a R-CPE (constant phase element). The CPE is generally used  
11  
12 to represent a distribution of relaxation times.<sup>42</sup> Fitting parameters are displayed in  
13  
14 Table 4. Capacitance values similar to the reported ones for single wall carbon nanotube  
15  
16 networks<sup>37</sup> were obtained.  
17  
18

19  
20 Fig 5(b) shows the evolution of SWNT bundles and junctions resistivities with  
21  
22 temperature from room temperature to 160 °C. A significant difference between them in  
23  
24 the whole range of temperatures, with quite higher resistivity values for the junctions, is  
25  
26 observed. It has been shown that the junction resistance is strongly dependent on the  
27  
28 size of the interconnecting bundles, with the smallest values associated with individual  
29  
30 tubes.<sup>39</sup> Thus, the high junction resistivity observed in this study is clearly pointing to  
31  
32 junctions involving large diameter bundles or SWNT agglomerates, which will control  
33  
34 the overall conductivity properties of the composite, as remarked by previous authors.<sup>39</sup>  
35  
36 Decreasing the bundle diameter will reduce the junction resistivity, and will increase the  
37  
38 composite conductivity. Future works will be devoted to further SWNT debundling.  
39  
40  
41

42  
43 It is also observed that whereas the SWNT bundles resistivity is almost constant  
44  
45 with temperature, a remarkable decrease of junctions' resistivity is observed with  
46  
47 increasing temperature. This behaviour is in good agreement with Sheng's theory of  
48  
49 fluctuation-induced electron tunnelling,<sup>43</sup> model that has been successfully applied to  
50  
51 describe the primary conduction mechanism across nanotube-nanotube junctions in  
52  
53 CNT composites.<sup>23,24</sup> Briefly, a system of SWNTs, such a rope or mat, can be  
54  
55 considered as containing many conducting regions separated by small insulating  
56  
57 barriers. In such a system, these tiny barriers will be very susceptible to charge  
58  
59  
60  
61  
62  
63  
64  
65

1  
2  
3  
4 fluctuations, resulting in electric field fluctuations across the tunneling junctions. These  
5  
6 fluctuations increase with increasing temperature, and the system conductivity can be  
7  
8 described by Sheng's formula  
9

$$\sigma = \sigma_0 \exp\left(\frac{-T_1}{T + T_0}\right) \quad (5)$$

10  
11  
12  
13  
14  
15 where  $\sigma_0$  is a preexponential constant, and  $T_0$  and  $T_1$  are the tunneling parameters,  
16  
17 which has previously been used to explain conductivity behaviour for carbon nanotube  
18  
19 systems.<sup>23,24</sup>  
20

21  
22 Figure 6 shows impedance complex plane plots corresponding to the composite  
23  
24 with 1.5 vol% SWNT from 200 to 400 °C. Two impedance arcs can be observed, which  
25  
26 behave surprisingly in a very different way. Whereas the arc at higher frequency  
27  
28 decreases monotonously with temperature, the arc at lower frequency increases up to  
29  
30 350 °C (arc not shown) and decreases for higher temperatures.  
31

32  
33 Two impedance arcs were also obtained when characterizing the monolithic  
34  
35 3YTZP ceramic and the composites with 0.5 and 1 vol% SWNT (not shown), the higher  
36  
37 frequency one corresponding to conductivity through the ceramic bulk and the lower  
38  
39 frequency one corresponding to conductivity through the grain boundaries. However, in  
40  
41 these two composites the conductivity evolution with temperature is the typical of an  
42  
43 ionic conductor, and both arcs decrease monotonously when increasing temperature,  
44  
45 resulting in an increase of conductivity both through the bulk and through the grain  
46  
47 boundaries.  
48  
49  
50

51  
52 In the case of the composite with 1.5 vol% SWNT, the arc at higher frequency  
53  
54 would contain the ionic contribution to conductivity through the ceramic bulk and also  
55  
56 the electronic one through the SWNT network. The second arc would be related to the  
57  
58 ionic conductivity through the grain boundaries, but in this case the fact that a great  
59  
60  
61  
62  
63  
64  
65

1  
2  
3  
4 fraction of the grain boundaries is covered by SWNTs reduces the ionic conductivity  
5  
6 resulting in an increase of the grain boundary resistivity for temperatures up to 350 °C,  
7  
8 and thus, an increase of the arc. For higher temperatures this effect is overcome and the  
9  
10 grain boundary conductivity increases with temperature. Equivalent circuit approach of  
11  
12 these data in order to obtain conductivity values for the different contributions presents  
13  
14 a high complexity and will be addressed in future studies.

15  
16  
17 Figure 7 shows the Arrhenius plots for total conductivity in the studied  
18  
19 composites, together with monolithic zirconia. **Total resistivity was calculated from**  
20  
21 **resistance values obtained from intercepts on the real, Z', axis.** The slope of these  
22  
23 diagrams was used to calculate the activation energy of the conducting species (Table  
24  
25 3). For composites with 0.5 and 1 vol% SWNT, as well as monolithic zirconia, a value  
26  
27 close to 0.8 eV was obtained. This result is consistent with the activation energy for  
28  
29 oxygen vacancy conduction in zirconia-based ceramic oxides.<sup>44,45,46</sup> Thus, these two  
30  
31 composites behave as ionic conductors without SWNT percolation. For the composite  
32  
33 with 1.5 vol% SWNT, a completely different behaviour was observed, with activation  
34  
35 energy of 65 meV, revealing that SWNT contribution to charge transport dominates for  
36  
37 temperatures up to 350 °C. In this case, an ionic-electronic mixed conductor is obtained  
38  
39 due to the percolated SWNT network. A similar result was reported for composites of 8  
40  
41 mol% Y<sub>2</sub>O<sub>3</sub>/ZrO<sub>2</sub> with SWNTs<sup>24</sup>, with activation energy of 30 meV.  
42  
43  
44  
45  
46  
47

#### 48 **4. Conclusions**

49  
50 Fully dense 3 mol% yttria doped zirconia matrix composites containing 0.5, 1  
51  
52 and 1.5 vol% SWNT, with equiaxed grain microstructure and almost analogous ceramic  
53  
54 grain size (250 nm), were prepared by colloidal processing and SPS. SWNTs were  
55  
56 homogeneously distributed at grain boundaries and also into large SWNT agglomerates.  
57  
58 Similar agglomerate mean size and shape were found for the three composites.  
59  
60  
61  
62  
63  
64  
65



1  
2  
3  
4 Increasing SWNT vol% leads to similar percentage of the total SWNT content  
5  
6 contained in agglomerates (~30%), and an increasing SWNT content at the grain  
7  
8 boundaries.  
9

10  
11 Similar Vickers hardness and slightly enhanced fracture toughness were  
12  
13 obtained for the composites in comparison with the monolithic 3YTZP ceramic. The  
14  
15 increase in the surface density of agglomerates does not play a fundamental role in their  
16  
17 evolution when increasing SWNT content.  
18

19  
20 Percolation threshold of the carbon nanotubes in the 3YTZP matrix was  
21  
22 estimated to be between 0.74 and 1.1 vol% SWNT corresponding to nominal contents  
23  
24 of 1 and 1.5 vol%, respectively. Composites with 0.5 and 1 vol% SWNT behaved as  
25  
26 ionic conductors without SWNT percolation, with ~0.8 eV activation energy.  
27  
28

29  
30 Room temperature conductivity in the composite with 1.5 vol% SWNT revealed  
31  
32 the existence of a percolated SWNT network in this material, which presented a mixed  
33  
34 ionic-electronic conduction with 65 meV activation energy. Modelling of impedance  
35  
36 properties in this composite using an equivalent circuit allowed separation of the  
37  
38 individual SWNT bundles contribution to resistance from the resistance due to junctions  
39  
40 between bundles. The existence of junctions involving large diameter bundles or SWNT  
41  
42 agglomerates resulted in higher junction resistivity in comparison with the SWNT  
43  
44 bundles resistivity. The remarkable decrease of junctions' resistivity with increasing  
45  
46 temperature up to 160 °C was successfully described in terms of the fluctuation-induced  
47  
48 electron tunnelling across nanotube-nanotube junctions.  
49  
50  
51  
52  
53

#### 54 **Acknowledgements**

55  
56 The authors acknowledge the financial support provided by the Spanish Ministry  
57  
58 of Science and Innovation (MAT2012-34217) and Junta de Andalucía (P12-FQM-  
59  
60  
61  
62  
63  
64  
65

1  
2  
3  
4  
5  
6  
7  
8  
9  
10  
11  
12  
13  
14  
15  
16  
17  
18  
19  
20  
21  
22  
23  
24  
25  
26  
27  
28  
29  
30  
31  
32  
33  
34  
35  
36  
37  
38  
39  
40  
41  
42  
43  
44  
45  
46  
47  
48  
49  
50  
51  
52  
53  
54  
55  
56  
57  
58  
59  
60  
61  
62  
63  
64  
65

1079). Microscopy studies have been performed in facilities belonging to the CITIUS  
(Universidad de Sevilla).

1  
2  
3  
4 **Figure captions**  
5  
6  
7

8 **Figure 1:** Raman spectra measured in the composites including the RBM frequency  
9 range and the D and G-Bands frequency range. Raman spectra measured in the  
10 monolithic 3YTZP ceramic and in the SWNTs have been included for comparison.  
11  
12  
13  
14

15  
16  
17 **Figure 2:** HRSEM micrographs of fracture surface of the composites with different  
18 SWNT contents (a) 0.5 vol%, (b) 1 vol%, and (c) 1.5 vol%.  
19  
20  
21  
22

23  
24 **Figure 3:** SEM micrographs showing the SWNT agglomerate distribution on the cross-  
25 sections of composites with different SWNT contents (a) 0.5 vol%, (b) 1 vol%, and (c)  
26 1.5 vol%.  
27  
28  
29  
30

31  
32  
33 **Figure 4:** (a) Vickers Hardness and (b) fracture toughness for monolithic 3YTZP and  
34 SWNT/3YTZP composites and comparisons with the bibliography values.  
35  
36  
37  
38

39  
40 **Figure 5:** (a) Impedance plots acquired in the composite with 1.5 vol% SWNT from  
41 room temperature to 180 °C and (b) SWNT bundles and junctions resistivity in this  
42 temperature range. The inset in (a) shows the equivalent circuit used to fit the  
43 impedance data.  
44  
45  
46  
47  
48  
49

50  
51 **Figure 6:** Impedance plots acquired in the composite with 1.5 vol% SWNT from 200 to  
52 400 °C.  
53  
54  
55  
56  
57  
58  
59  
60  
61  
62  
63  
64  
65

1  
2  
3  
4  
5  
6  
7  
8  
9  
10  
11  
12  
13  
14  
15  
16  
17  
18  
19  
20  
21  
22  
23  
24  
25  
26  
27  
28  
29  
30  
31  
32  
33  
34  
35  
36  
37  
38  
39  
40  
41  
42  
43  
44  
45  
46  
47  
48  
49  
50  
51  
52  
53  
54  
55  
56  
57  
58  
59  
60  
61  
62  
63  
64  
65

**Figure 7:** Arrhenius plots of the electrical conductivity for monolithic 3YTZP and 3YTZP/SWNT composites.

**Table 1:** Theoretical and relative density and morphological parameters for ceramic grains in monolithic 3YTZP and SWNT/3YTZP composites.

<b>SWNT vol%</b>	<b><math>\rho_{th}</math></b> <b>(g·cm<sup>-3</sup>)</b>	<b><math>\rho_r</math></b> <b>(%)</b>	<b>&lt;d&gt;</b> <b>(nm)</b>	<b><math>\sigma_{&lt;d&gt;}</math></b> <b>(nm)</b>	<b>f</b>
0	6.10	100	215	85	0.75±0.08
0.5	6.08	100	230	80	0.74±0.08
1	6.06	100	215	75	0.73±0.06
1.5	6.04	99.4	240	80	0.76±0.05

**Table 2:** Surface density of SWNT agglomerates, percentage of carbon nanotube content in agglomerates and at grain boundaries calculated for each composite and morphological parameters of agglomerates.

SWNT vol%	$\rho_s$ (%)	A (%)	A-SWNT vol%	GB-SWNT vol%	$\langle D \rangle$ ( $\mu\text{m}$ )	$\sigma_{\langle D \rangle}$ ( $\mu\text{m}$ )	$D_{\text{máx}}$ ( $\mu\text{m}$ )	F
0.5	$0.18 \pm 0.07$	36	0.18	0.32	9	7	60	$0.4 \pm 0.3$
1	$0.26 \pm 0.03$	26	0.26	0.74	7	4	30	$0.5 \pm 0.2$
1.5	$0.40 \pm 0.05$	27	0.40	1.10	8	5	40	$0.5 \pm 0.2$

**Table 3:** Mechanical and electrical properties measured for the studied materials.

<b>SWNT vol%</b>	<b><math>H_V</math> (GPa)</b>	<b><math>K_{IC}</math> (MPa·m<sup>1/2</sup>)</b>	<b><math>\sigma_{RT}</math> (S·cm<sup>-1</sup>)</b>	<b><math>E_{act}</math> (eV)</b>
0	12.7±0.4	4.3±0.3	----	0.86±0.02
0.5	13.4±0.3	4.2±0.3	----	0.84±0.08
1	12.6±0.2	4.4±0.2	----	0.76±0.07
1.5	12.9±0.3	4.6±0.3	6x10 <sup>-6</sup>	0.065±0.002

**Table 4:** Equivalent circuit values for the fitting of the impedance properties of the composite with 1.5 vol% SWNT.

T (°C)	$\rho_J$ (k $\Omega$ ·cm)	C <sub>J</sub> (pF)	$\rho_B$ (k $\Omega$ ·cm)	C <sub>B</sub> (pF)
25	158±13	272±3	10.4±0.9	137±3
40	135±11	279±3	9.1±0.8	139±4
60	113±10	293±4	7.8±0.7	139±4
80	93±7	302±4	6.9±0.5	137±4
100	83±6	318±4	6.4±0.5	136±4
120	76±6	340±6	6.5±0.6	132±4
140	70±5	351±5	6.1±0.4	132±4
160	66±6	400±8	6.4±0.6	135±4
180	56±5	475±1	6.6±0.6	128±5



1  
2  
3  
4 **References**  
5  
6  
7

- 
- 8  
9 <sup>1</sup> Baughman RH, Zakhidov AA, de Heer WA. Carbon nanotubes- the route toward  
10 applications. *Science* 2002; **297**: 787-92.  
11  
12 <sup>2</sup> Zhang Q, Huang JQ, Zhao MQ, Qian WZ, Wei F. Carbon nanotube mass production:  
13 principles and processes. *Chem Sus Chem* 2011; **4**: 864-89.  
14  
15 <sup>3</sup> Endo M, Strano MS, Ajayan PM. Potential applications of carbon nanotubes. *Top Appl*  
16 *Phys* 2008; **111**: 13-61.  
17  
18 <sup>4</sup> Schnorr JM, Swager TM. Emerging applications of carbon nanotubes. *Chem Mater*  
19 2011; **23**: 646-57.  
20  
21 <sup>5</sup> Zhang Q, Huang JQ, Qian WZ, Zhang YY, Wei F. *Small* 2013; **9**: 1237–65.  
22  
23 <sup>6</sup> Pature NP. Multifunctional composites of ceramics and single-walled carbon  
24 nanotubes. *Adv Mater* 2009; **21**: 1767–70.  
25  
26 <sup>7</sup> Deville S, Gremillard L, Chevalier J, Fantozzi G. A critical comparison of methods for  
27 the determination of the aging sensitivity in biomedical grade yttria-stabilized zirconia.  
28 *J Biomed Mater Res B Appl Biomater* 2005; **72**: 239–45.  
29  
30 <sup>8</sup> Minh NQ. Ceramic fuel cells. *J Am Ceram Soc* 1993; **76**: 563–88.  
31  
32 <sup>9</sup> Duszová A, Dusza J, Tomasek K, Blugan G, Kuebler J. Microstructure and properties  
33 of carbon nanotube/zirconia composite. *J Eur Ceram Soc* 2008; **28**: 1023–27.  
34  
35 <sup>10</sup> Garmendia N, Grandjean S, Chevalier J, Diaz LA, Torrecillas R, Obieta I. Zirconia-  
36 multiwall carbon nanotubes dense nano-composites with an unusual balance between  
37 crack and ageing resistance. *J Eur Ceram Soc* 2011; **31**: 1009–14.  
38  
39 <sup>11</sup> Shin JH, Hong SH. Microstructure and mechanical properties of single wall carbon  
40 nanotube reinforced yttria stabilized zirconia ceramics. *Mater Sci Eng A* 2012; **556**:  
41 382–7.  
42  
43  
44  
45  
46  
47  
48  
49  
50  
51  
52  
53  
54  
55  
56  
57  
58  
59  
60  
61  
62  
63  
64  
65

1  
2  
3  
4  
5 <sup>12</sup> Shen L, Han YH, Xiang C, Tang H, Mukherjee A, Kim S, Bae SI, Huang Q. Phase  
6 transformation behavior of ZrO<sub>2</sub> by addition of carbon nanotubes consolidated by spark  
7 plasma sintering. *Scripta Mater* 2013; **69**: 736–39.

8  
9  
10  
11 <sup>13</sup> Poyato R, Gallardo-López A, Gutiérrez-Mora F, Morales-Rodríguez A, Muñoz A,  
12 Domínguez-Rodríguez A. Effect of high SWNT content on the room temperature  
13 mechanical properties of fully dense 3YTZP/SWNT composites. *J Eur Ceram Soc*  
14 2014; **34**: 1571–79.

15  
16  
17  
18  
19  
20  
21 <sup>14</sup> Garmendia N, Santacruz I, Moreno R, Obieta I. Slip casting of  
22 nanozirconia/MWCNT composites using a heterocoagulation process. *J Eur Ceram Soc*  
23 2009; **29**:1939–45.

24  
25  
26  
27  
28  
29  
30  
31 <sup>15</sup> Chintapalli RK, Garcia Marro F, Milsom B, Reece M, Anglada M. Processing and  
32 characterization of high-density zirconia-carbon nanotube composites. *Mater Sci Eng A*  
33 2012; **549**: 50-9.

34  
35  
36  
37  
38  
39  
40  
41 <sup>16</sup> Kasperski A, Weibel A, Alkattan D, Estournès C, Turq V, Laurent Ch, Peigney A.  
42 Microhardness and friction coefficient of multi-walled carbon nanotube-yttria-stabilized  
43 ZrO<sub>2</sub> composites prepared by spark plasma sintering. *Scripta Mater* 2013; **69**: 338–41.

44  
45  
46  
47  
48  
49  
50  
51 <sup>17</sup> Bakhsh N, Ahmad Khalid F, Saeed Hakeem A. Synthesis and characterization of  
52 pressureless sintered carbon nanotube reinforced alumina nanocomposites. *Mater Sci*  
53 *Eng A* 2013; **578**: 422-29.

54  
55  
56  
57  
58  
59  
60  
61 <sup>18</sup> Zapata-Solvas E, Gómez-García D, Domínguez-Rodríguez A. Towards physical  
62 properties tailoring of carbon nanotubes-reinforced ceramic matrix composites. *J Eur*  
63 *Ceram Soc* 2012; **32**: 3001-20.

64  
65  
66  
67  
68  
69  
70  
71 <sup>19</sup> Morales-Rodríguez A, Gallardo-López A, Fernández-Serrano A, Poyato R, Muñoz A,  
72 Domínguez-Rodríguez A. Improvement of Vickers hardness measurement on

1  
2  
3  
4  
5 SWNT/Al<sub>2</sub>O<sub>3</sub> composites consolidated by spark plasma sintering. *J Eur Ceram Soc*  
6  
7 2014; **34**: 3801-09.

8  
9 <sup>20</sup> Rul S, Lefèvre-schlick F, Capria E, Laurent Ch, Peigney A. Percolation of single-  
10 walled carbon nanotubes in ceramic matrix nanocomposites. *Acta Mater* 2004; **52**:  
11 1061–67.

12  
13  
14  
15  
16 <sup>21</sup> Ahmad K, Pan W, Shi SL. Electrical conductivity and dielectric properties of  
17 multiwalled carbon nanotube and alumina composites. *Appl Phys Lett* 2006; **89**:  
18 133122.

19  
20  
21  
22  
23 <sup>22</sup> Shi SL, Liang J. Effect of multiwall carbon nanotubes on electrical and dielectric  
24 Properties of yttria-stabilized zirconia ceramic. *J Am Ceram Soc* 2006; **89**: 3533–35.

25  
26  
27  
28 <sup>23</sup> Shi SL, Lian J. Electronic transport properties of multiwall carbon nanotubes/yttria  
29 stabilized zirconia composites. *J Appl Phys* 2007; **101**: 023708.

30  
31  
32  
33  
34  
35 <sup>24</sup> Fonseca FC, Muccillo R, de Florio DZ, Ladeira LO, Ferlauto AS. Mixed ionic-  
36 electronic conductivity in yttria-stabilized zirconia/carbon nanotube composites. *Appl*  
37 *Phys Lett* 2007; **91**: 243107.

38  
39  
40  
41  
42  
43 <sup>25</sup> Ahmad K, Pan W. Dramatic effect of multiwalled carbon nanotubes on the electrical  
44 properties of alumina based ceramic nanocomposites. *Compos Sci Technol* 2009; **69**:  
45 1016–21.

46  
47  
48  
49  
50  
51 <sup>26</sup> González-Julián J, Iglesias Y, Caballero AC, Belmonte M, Garzón L, Ocal C,  
52 Miranzo P, Osendi MI. Multi-scale electrical response of silicon nitride/multi-walled  
53 carbon nanotubes composites. *Compos Sci Technol* 2011; **71**: 60–66.

54  
55  
56  
57  
58  
59  
60  
61 <sup>27</sup> Castillo-Rodríguez M, Muñoz A, Morales-Rodríguez A, Poyato R, Gallardo-López  
62 A, Domínguez-Rodríguez A. Influence of the processing route on the carbon nanotubes  
63 dispersion and creep resistance of 3YTZP/SWCNTs nanocomposites. *J Am Ceram Soc*  
64 2015; **98**: 645-53.  
65

1  
2  
3  
4  
5 <sup>28</sup> Poyato R, Vasiliev AL, Pature NP, Tanaka H, Nishimura T. Aqueous colloidal  
6 processing of single-wall carbon nanotubes and their composites with ceramics.  
7  
8 *Nanotechnol* 2006; **17**: 1770–77.  
9

10  
11 <sup>29</sup> Anstis GR, Chantikul P, Lawn DB, Marshall DB. A critical evaluation of indentation  
12 techniques for measuring fracture toughness: I. direct crack measurement. *J Am Ceram*  
13 *Soc* 1981; **64**: 533–38.  
14  
15

16  
17 <sup>30</sup> Li M, Feng Z, Xiang G, Ying P, Xin Q, Li C. Phase transformation in the surface  
18 region of zirconia detected by UV Raman spectroscopy. *J Phys Chem B* 2001; **105**:  
19 8107–11.  
20  
21

22  
23 <sup>31</sup> Zhou JP, Gong QM, Yuan KY, Wu JJ, Chen YF, Li CS, et al. The effects of  
24 multiwalled carbon nanotubes on the hot-pressed 3 mol% yttria stabilized zirconia  
25 ceramics. *Mater Sci Eng A* 2009; **520**:153–7.  
26  
27

28  
29 <sup>32</sup> Poorteman M, Traianidis M, Bister G, Cambier F. Colloidal processing, hot pressing  
30 and characterisation of electroconductive MWCNT-alumina composites with  
31 compositions near the percolation threshold. *J Eur Ceram Soc* 2009; **29**: 669–75  
32  
33

34  
35 <sup>33</sup> Zhang SC, Fahrenholtz WG, Hilmas GE, Yadlowsky EJ. Pressureless sintering of  
36 carbon nanotube–Al<sub>2</sub>O<sub>3</sub> composites. *J Eur Ceram Soc* 2010; **30**: 1373–80.  
37  
38

39  
40 <sup>34</sup> Gallardo-López A, Poyato R, Morales-Rodríguez A, Fernández-Serrano A, Muñoz A,  
41 Domínguez-Rodríguez A. Hardness and flexural strength of single-walled carbon  
42 nanotube/alumina composites. *J Mater Sci* 2014; **49**: 7116–23.  
43  
44

45  
46 <sup>35</sup> **Cho J, Inam F, Reece MJ, Chlup Z, Dlouhy I, Shaffer MSP, et al. Carbon**  
47 **nanotubes: do they toughen brittle matrices?. *J Mater Sci* 2011; 46: 4770–9.**  
48  
49

50  
51 <sup>36</sup> **Mazaheri M, Mari D, Razavi Hesabi Z, Schaller R, Fantozzi G. Multi-walled**  
52 **carbon nanotube/nanostructured zirconia composites: outstanding mechanical**  
53 **properties in a wide range of temperature. *Compos Sci Technol* 2011; 71: 939–45.**  
54  
55  
56  
57  
58  
59  
60  
61  
62  
63  
64  
65

1  
2  
3  
4  
5 <sup>37</sup> Garret MP, Ivanov IN, Gerhardt RA, Puretzky AA, Geohegan DB. Separation of  
6  
7 junction and bundles resistance in single wall carbon nanotube percolation networks by  
8  
9 impedance spectroscopy. *Appl Phys Lett* 2010; **97**: 163105.

10  
11 <sup>38</sup> Louie SG: Electronic properties, junctions, and defects of carbon nanotubes, in  
12  
13 Carbon Nanotubes: Synthesis, Structure, Properties, and Applications, Vol. 80, edited  
14  
15 by M.S. Dresselhaus, G. Dresselhaus and P. Avouris (Springer, Berlin, 2001), p. 113.

16  
17 <sup>39</sup> Nirmalraj PN, Lyons PE, De S, Coleman JN, Boland JJ. Electrical Connectivity in  
18  
19 Single-Walled Carbon Nanotube Networks. *Nano Letters* 2009; **9**: 3890-95.

20  
21 <sup>40</sup> Li C, Thostenson ET, Chou TW. Dominant role of tunneling resistance in the  
22  
23 electrical conductivity of carbon nanotube-based composites. *Appl Phys Lett* 2007; **91**:  
24  
25 223114.

26  
27 <sup>41</sup> Muhlbauer RL, Pruyn TL, Puckett WT, Gerhardt RA. Effect of graphitic filler size  
28  
29 and shape on the microstructure, electrical percolation behavior and thermal properties  
30  
31 of nanostructured multilayered carbon films deposited onto paper substrates. *J Mater*  
32  
33 *Res* 2014; **29**: 472-84.

34  
35 <sup>42</sup> Macdonald JR. Impedance spectroscopy. *Ann Biomed Eng* 1992; **20**: 289-305.

36  
37 <sup>43</sup> Sheng P. Fluctuation-induced tunneling conduction in disordered materials. *Phys Rev*  
38  
39 *B* 1980; **21**: 2180-95.

40  
41 <sup>44</sup> Guo X, Waser R. Electrical properties of the grain boundaries of oxygen ion  
42  
43 conductors: Acceptor-doped zirconia and ceria. *Progr Mater Sci* 2006; **51**: 151-210.

44  
45 <sup>45</sup> Bernard-Granger G, Guizard C, Surblé S, Baldinozzi G, Addad A. Spark plasma  
46  
47 sintering of a commercially available granulated zirconia powder-II. Microstructure  
48  
49 after sintering and ionic conductivity. *Acta Mater* 2008; **56**: 4658-72.

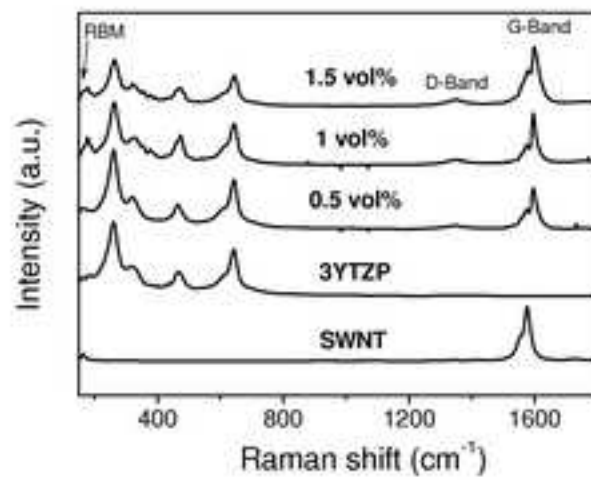
1  
2  
3  
4  
5  
6  
7  
8  
9  
10  
11  
12  
13  
14  
15  
16  
17  
18  
19  
20  
21  
22  
23  
24  
25  
26  
27  
28  
29  
30  
31  
32  
33  
34  
35  
36  
37  
38  
39  
40  
41  
42  
43  
44  
45  
46  
47  
48  
49  
50  
51  
52  
53  
54  
55  
56  
57  
58  
59  
60  
61  
62  
63  
64  
65

---

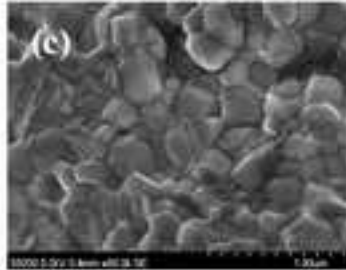
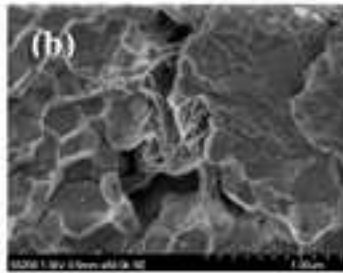
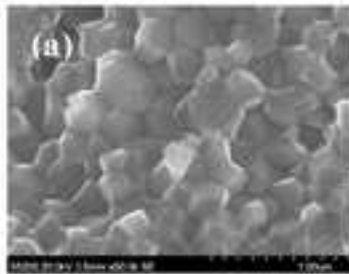
<sup>46</sup> Perry NH, Mason TO. Grain core and grain boundary electrical/dielectric properties of yttria-doped tetragonal zirconia polycrystal (TZP) nanoceramics. *Solid State Ionics* 2010; **181**: 276-84.

Figure 1

[Click here to download high resolution image](#)



**Figure 2**  
[Click here to download high resolution image](#)





**Figure 3**  
[Click here to download high resolution image](#)

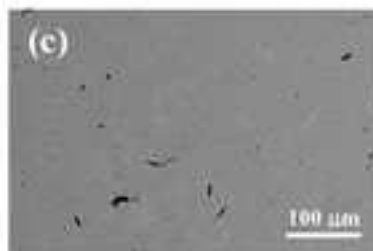
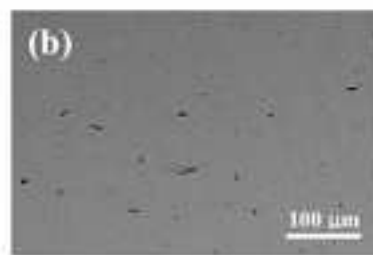
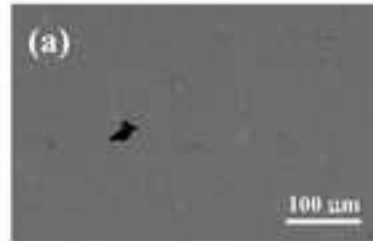


Figure 4

[Click here to download high resolution image](#)

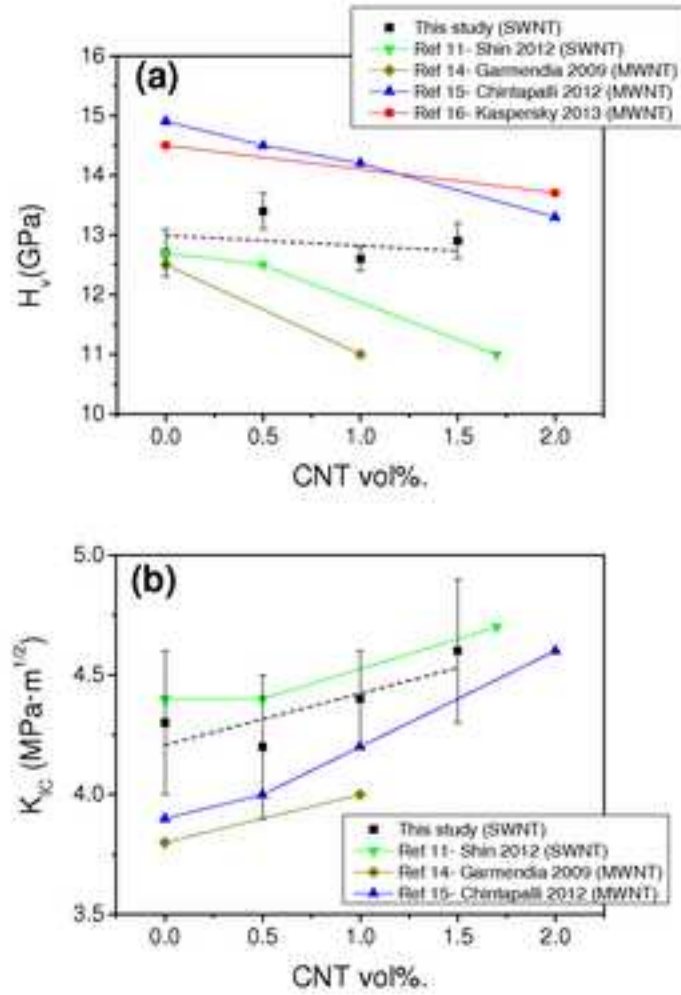


Figure 5

[Click here to download high resolution image](#)

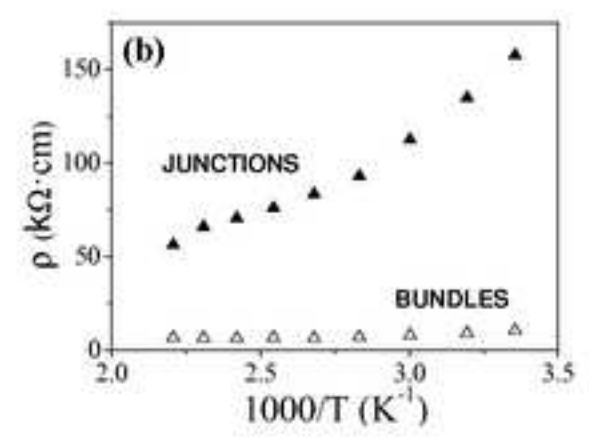
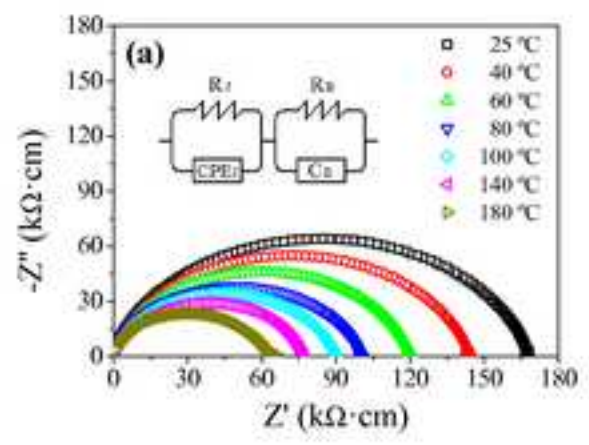


Figure 6  
[Click here to download high resolution image](#)

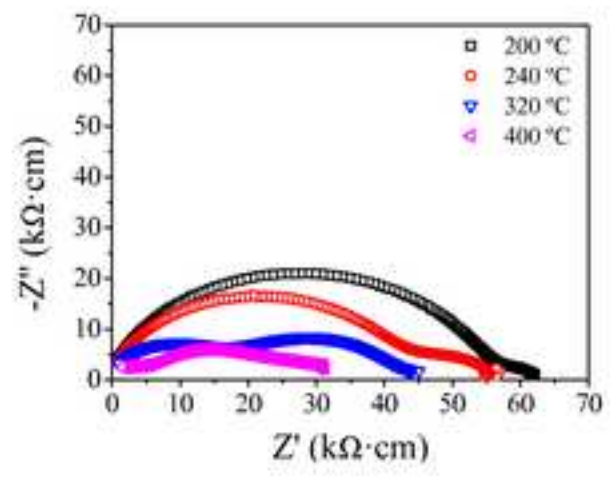
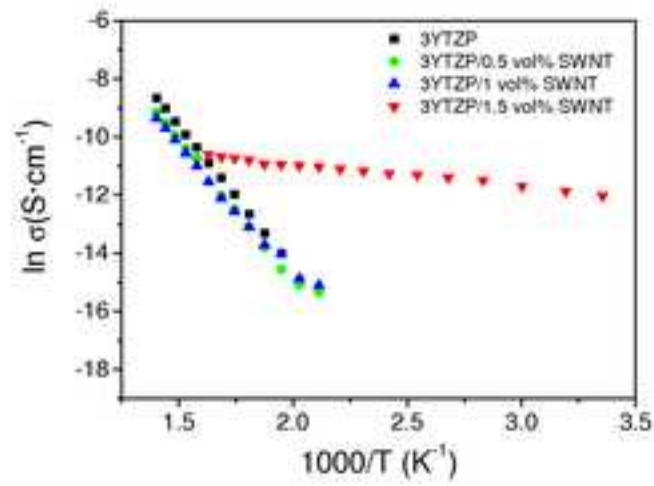


Figure 7  
[Click here to download high resolution image](#)



1  
2  
3  
4  
5  
6  
7  
8  
9  
10  
11  
12  
13  
14  
15  
16  
17  
18  
19  
20  
21  
22  
23  
24  
25  
26  
27  
28  
29  
30  
31  
32  
33  
34  
35  
36  
37  
38  
39  
40  
41  
42  
43  
44  
45  
46  
47  
48  
49  
50  
51  
52  
53  
54  
55  
56  
57  
58  
59  
60  
61  
62  
63  
64  
65

**Figure 1:** Raman spectra measured in the composites including the RBM frequency range and the D and G-Bands frequency range. Raman spectra measured in the monolithic 3YTZP ceramic and in the SWNTs have been included for comparison.

**Figure 2:** HRSEM micrographs of fracture surface of the composites with different SWNT contents (a) 0.5 vol%, (b) 1 vol%, and (c) 1.5 vol%.

**Figure 3:** SEM micrographs showing the SWNT agglomerate distribution on the cross-sections of composites with different SWNT contents (a) 0.5 vol%, (b) 1 vol%, and (c) 1.5 vol%.

**Figure 4:** (a) Vickers Hardness and (b) fracture toughness for monolithic 3YTZP and SWNT/3YTZP composites and comparisons with the bibliography values.

**Figure 5:** (a) Impedance plots acquired in the composite with 1.5 vol% SWNT from room temperature to 180 °C and (b) SWNT bundles and junctions resistivity in this temperature range. The inset in (a) shows the equivalent circuit used to fit the impedance data.

**Figure 6:** Impedance plots acquired in the composite with 1.5 vol% SWNT from 200 to 400 °C.

**Figure 7:** Arrhenius plots of the electrical conductivity for monolithic 3YTZP and 3YTZP/SWNT composites.